



# Exploring the mechanisms leading to diffuse and filamentary modes in dielectric barrier discharges in N<sub>2</sub> with N<sub>2</sub>O admixtures

Hans Höft<sup>1,a</sup> , Markus M. Becker<sup>1</sup> , Manfred Kettlitz<sup>1</sup> , Simon Dap<sup>2</sup> , Nicolas Naudé<sup>2</sup> , Ronny Brandenburg<sup>1,3</sup> , and Klaus-Dieter Weltmann<sup>1</sup> 

<sup>1</sup> Leibniz Institute for Plasma Science and Technology (INP), Felix-Hausdorff-Str. 2, 17489 Greifswald, Germany

<sup>2</sup> LAPLACE, Université de Toulouse, CNRS, INPT, UPS, Toulouse, France

<sup>3</sup> Institute of Physics, University of Rostock, Albert-Einstein-Str. 23–24, 18059 Rostock, Germany

Received 11 November 2022 / Accepted 16 January 2023 / Published online 2 March 2023  
© The Author(s) 2023

**Abstract.** The effects of nitrous oxide (N<sub>2</sub>O) in nitrogen (N<sub>2</sub>) on the development and morphology of sine-driven dielectric barrier discharges in a single-filament arrangement were studied. Detailed insight in the characteristics of the discharge and its development were obtained from electrical measurements combined with ICCD and streak camera recordings as well as numerical modelling. A miniaturised atmospheric pressure Townsend discharge (APTD) could be generated for admixtures up to 5 vol% N<sub>2</sub>O in N<sub>2</sub> although N<sub>2</sub>O is an efficient collisional quencher of metastable nitrogen molecules. Increasing the high voltage amplitude led to a transition into a hybrid mode with the generation of an intermediate filament in addition to the diffuse, non-constricted APTD. A time-dependent, spatially one-dimensional fluid model was applied in order to study the underlying mechanisms causing the diffuse discharge characteristics. It was found that even for small N<sub>2</sub>O admixtures, the associative ionisation of atomic nitrogen and oxygen ( $O + N(^2P) \rightarrow NO^+ + e$ ) is the major electron source sustaining the volume memory effect and is therefore the reason for the formation of a diffuse APTD.

## 1 Introduction

The dielectric barrier discharge (DBD) as a non-thermal atmospheric pressure plasma source is receiving increasing attention during the last 30 years, in both research and industrial applications. First investigated in the second half of the nineteenth century, DBDs obtained wide use as the “ozonizer discharges” and later as “corona surface treater”, in light sources, air cleaning and for the pumping of gas lasers [1]. Today, they are still under study for e.g. life-science applications, layer deposition, gas cleaning and conversion, aerodynamic flow control or analytic detection devices. With the increasing interest in this type of gas discharge from the 1990s onwards, the number of publications increased. The book “*Non-Equilibrium Air Plasmas At Atmospheric Pressure*” edited by Kurt H. Becker with Ulrich Kogelschatz, Karl H. Schoenbach and Robert J. Barker in 2005 was an important milestone [1]. Being one of the first textbooks about DBDs, it provides a

broad overview and is still an excellent introduction to the subject. Furthermore, the new topic of “microplasmas” was also developed at that time [2].

Non-thermal plasmas generated by DBDs are usually filamentary [3], but at specific conditions, diffuse or uniform discharges are obtained [4–9]. These diffuse DBDs are attractive for surface deposition applications, as linear processing with less sophisticated vacuum technology can be realised while enabling a homogeneous surface treatment [10, 11]. Diffuse DBDs are distinguished between atmospheric pressure Townsend discharges (APTDs) and atmospheric pressure glow discharges (APGDs) with intermediate modes, which depend mainly on the frequency and amplitude of the applied voltage waveform [12–14]. APTDs are mainly generated in sinusoidal-operated planar DBD arrangements in N<sub>2</sub>, pure or with small (i.e. up to about 500 ppm) admixtures of O<sub>2</sub> or N<sub>2</sub>O, or under certain conditions even in atmospheric pressure air [15]. An example for a miniaturised APTD in a “single-filament” arrangement in N<sub>2</sub> with and without O<sub>2</sub> admixtures can be found in [16]. Volume and surface memory effects are supposed to determine the discharge regime [4, 6, 17–19]. These memory effects increase the number of electrons prior and during the breakdown. Consequently, the discharge ignites at low electrical field

Electron-Driven Processes from Single Collisions to High-Pressure Plasmas.

Guest editors: Jose L Lopez, Michael Brunger, Holger Kersten.

<sup>a</sup> e-mail: [hans.hoefl@inp-greifswald.de](mailto:hans.hoefl@inp-greifswald.de) (corresponding author)

strength and its formation proceeds slower than in case of streamer generation [17]. For the APTD in  $N_2$  mainly the spontaneous electron emission and secondary electron emission induced by  $N_2(A^3\Sigma_u^+)$  were considered to be responsible for the memory effect [20–23]. The role of the latter process is evident due to the fact that small additions of  $N_2(A^3\Sigma_u^+)$  quenchers (e.g.  $O_2$  or  $NH_3$ ) limit the frequency range at which APTDs occur [16, 17]. A full understanding of the underlying physics of discharge formation is still missing, especially for conditions important for layer deposition. In particular, the control of discharge uniformity in gas mixtures containing precursor molecules and reactive components is rarely studied.  $N_2O$  is interesting for such studies from several viewpoints, namely as an electronegative compound, as an oxidising agent, and as a donor of oxygen atoms during thin film deposition.

In a previous work, the impact of nitrous oxide ( $N_2O$ ) admixture to  $N_2$  on DBD characteristics was studied in a pulsed operated, single-filament arrangement [24]. Under pulsed operation, these DBDs were found to be filamentary both for virtually pure  $N_2$  as well as for all used  $N_2O$  concentrations in  $N_2$  (up to 10 vol%), i.e. the diffuse discharge regimes could not be generated and examined. Therefore, the focus of this work is the investigation of sine-driven DBDs using the same arrangement and gas compositions to test if the APTD mode can also be generated in such a single-filament configuration. Furthermore, the transition to a filamentary operation is of high interest for understanding underlying mechanisms and eventually the evaluation of potential applications. The focus of the experimental analysis lies therefore on fast optical diagnostics (ICCD and streak camera) to identify the occurrence of APTDs and track their faint emission. These methods were accompanied by fast electrical measurements. For the identification of the mechanisms responsible for the transition to a diffuse APTD mode a time-dependent 1D fluid model was applied, investigating especially the role of metastable  $N_2(A^3\Sigma_u^+)$ , atomic oxygen, and atomic nitrogen on the volume memory effect.

## 2 Experimental set-up and model description

### 2.1 Discharge arrangement and diagnostics

The same discharge arrangement as in the previous study on the impact of  $N_2O$  in  $N_2$  for pulsed operation described in [24] was used, together with similar diagnostics (see Fig. 1). Therefore, only the essential details are briefly given here.

A symmetric double-sided DBD arrangement with half-spherical, alumina-covered metal electrodes with a gap width of 1 mm was used (Fig. 2). The alumina-covered electrodes had a diameter of about 4 mm and a tip radius of about 2 mm. The thickness of the dielectric above the tip was about 0.5 mm. The electrodes were

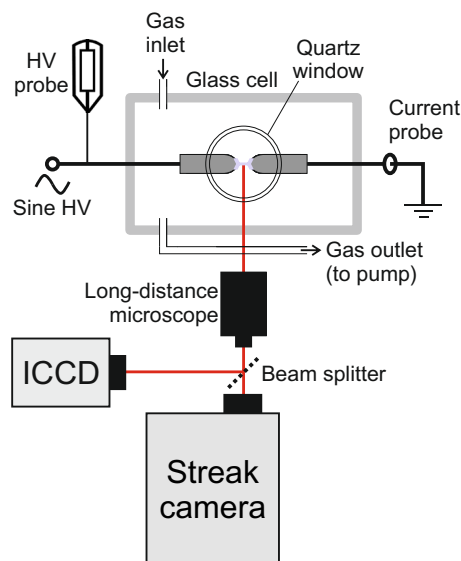


**Fig. 1** Scheme of the experimental setup

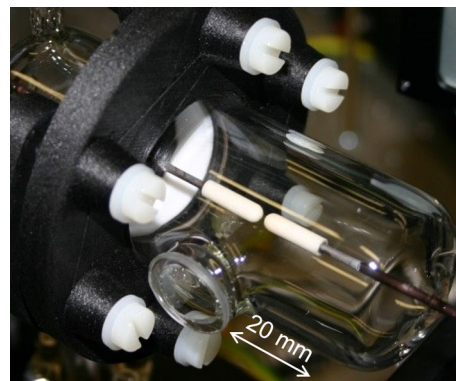


**Fig. 2** Discharge cell with a quartz window and alumina-covered, half-spherical electrodes with a 1 mm gap

placed in a vacuum tight glass cell (Fig. 2). The cell was evacuated by a turbo pump (Pfeiffer TSH261) down to about  $10^{-6}$  mbar before filling the cell with the gas. An additional membrane pump (Pfeiffer MVP 020-3 AC) was used as a process pump in a bypass to set the pressure in the cell to 1 bar. The total gas flow through the cell was set to 100 sccm by mass flow controllers connected to gas cylinders ( $N_2$ , purity 5.0, i.e. 99.999% purity). The investigated gas mixtures were varied from virtually pure  $N_2$  to 10 vol%  $N_2O$  in  $N_2$ . “Virtually pure  $N_2$ ” means  $\leq 30$  ppm  $O_2$  impurity (which is already affecting the APTD behaviour [22]) as examined by an oxygen sensor (Zirox SGM 7.4).

A custom-built sinusoidal high-voltage (HV) power supply (push-pull generator with HV transformer) generating up to  $14\text{ kV}_{pp}$  at 10 kHz frequency ( $f_{rep}$ ) was used for the operation of the DBDs. The structure and the spatio-temporal development of the DBDs were recorded in the UV and visible spectral range by a fast ICCD camera (Andor iStar DH734-18U-A3) through a quartz glass window (see Fig. 2). The spatial resolution

**Table 1** Heavy particle species considered in the reaction kinetic model. Species denoted with ‘\*’ represent lumped excited states at the given kinetic energy

<i>Neutrals in ground state</i>	
O, O <sub>2</sub> , O <sub>3</sub>	
N, N <sub>2</sub>	
NO, NO <sub>2</sub> , NO <sub>3</sub>	
N <sub>2</sub> O, N <sub>2</sub> O <sub>5</sub>	
<i>Neutrals in vibrationally excited state at level <math>\nu</math></i>	
O <sub>2</sub> (X <sup>3</sup> $\Sigma_g^-$ , $\nu = 1, \dots, 4$ )	
N <sub>2</sub> (X <sup>1</sup> $\Sigma_g^+$ , $\nu = 1, \dots, 10$ )	
<i>Neutrals in electronically excited state</i>	
O( <sup>1</sup> D), O*(4.19 eV)	
O <sub>2</sub> (a <sup>1</sup> $\Delta_g$ ), O <sub>2</sub> (b <sup>1</sup> $\Sigma_g^+$ ), O <sub>2</sub> * (4.50 eV)	
O <sub>3</sub> * (1.77 eV)	
N( <sup>2</sup> D), N( <sup>2</sup> P)	
N <sub>2</sub> (A <sup>3</sup> $\Sigma_u^+$ ), N <sub>2</sub> (B <sup>3</sup> $\Pi_g$ ), N <sub>2</sub> (B' <sup>3</sup> $\Sigma_u^-$ )	
N <sub>2</sub> (a' <sup>1</sup> $\Sigma_u^-$ ), N <sub>2</sub> (a <sup>1</sup> $\Pi_g$ ), N <sub>2</sub> (C <sup>3</sup> $\Pi_u$ ), N <sub>2</sub> (a'' <sup>1</sup> $\Sigma_g^+$ )	
NO(A <sup>2</sup> $\Sigma^+$ ), NO(B <sup>2</sup> $\Pi$ ), NO <sub>2</sub> (A)	
<i>Positive ions</i>	
O <sup>+</sup> , O <sub>2</sub> <sup>+</sup> , O <sub>3</sub> <sup>+</sup> , O <sub>4</sub> <sup>+</sup>	
N <sup>+</sup> , N <sub>2</sub> <sup>+</sup> , N <sub>3</sub> <sup>+</sup> , N <sub>4</sub> <sup>+</sup>	
NO <sup>+</sup> , NO <sub>2</sub> <sup>+</sup> , N <sub>2</sub> O <sup>+</sup>	
<i>Negative ions</i>	
O <sup>-</sup> , O <sub>2</sub> <sup>-</sup> , O <sub>3</sub> <sup>-</sup> , O <sub>4</sub> <sup>-</sup>	
NO <sup>-</sup> , NO <sub>2</sub> <sup>-</sup> , NO <sub>3</sub> <sup>-</sup> , N <sub>2</sub> O <sup>-</sup>	

was about 2  $\mu\text{m}$ , while the maximal temporal resolution was 2 ns. A streak-camera system (HAMAMATSU C5680-21C) recorded the spatio-temporal development of the DBDs with about 2  $\mu\text{m}$  spatial and about 20 ps temporal resolution. The high spatial resolution was enabled by a long-distance microscope (Questar QM100). More details on the optical diagnostics can be found in [24, 25]. Electrical measurements were performed with current and voltage probes and recorded with an oscilloscope (Tektronix DPO 7254C). The high frequency current transformer (MagneLab CT-F2.5 BNC) provided a high sensitivity (2.5 V/A) with a rise time of 0.7 ns and a bandwidth range between 1.2 kHz and 500 MHz. The voltage probe (Tektronix P6015A) had a bandwidth of 75 MHz.

## 2.2 Numerical model

The same time-dependent, spatially one-dimensional fluid model as used in [26] was applied here to support the interpretation of the experimental results.

From measured data, only the applied voltage at the HV electrode was used as an input (in addition to the geometry of the discharge arrangement on the central axis, i.e. 1 mm gap and 0.5 mm dielectric thickness). The Poisson equation and several balance equations were self-consistently solved as described in [27].

While the Poisson equation delivered the potential and the axial electric field, the particle densities and the energy density of the electrons were calculated by the balance equations. The fluxes of heavy particles were determined in the common drift-diffusion approximation as described in [27]. For the particle and energy flux of the electrons, an improved drift-diffusion approximation, see [28], was used. The accumulation of surface charges at the dielectric surfaces was accounted for by the addition of charged particle fluxes. The reaction kinetics scheme was based on [29] and included about 50 heavy particle species (see Table 1)<sup>1</sup> and more than 520 reactions. Besides the N<sub>2</sub>O admixture to N<sub>2</sub>, an O<sub>2</sub> concentration of 30 ppm was considered to account for the experimentally unavoidable impurity. The secondary emission of electrons from the dielectric surfaces by N<sub>2</sub>(A) impact was considered with a secondary electron emission coefficient of 0.2. This value appears to be an upper limit for the secondary electron emission occurring during the collision of metastable nitrogen molecules with dielectric surfaces [30]. Besides, the partial reflection and emission of particles according to [31] was used as boundary condition at the dielectrics with a secondary electron emission coefficient for ion-induced electron emission of 0.02. A quasi-neutral state with an electron density of 10<sup>3</sup> cm<sup>-3</sup> was used as initial condition.

## 3 Results and discussion

While varying the N<sub>2</sub>O concentration in N<sub>2</sub> in the DBD arrangement under consideration, two different discharge regimes were found in dependence on the amplitude of the sinusoidal HV at 10 kHz:

- i. Diffuse regime: pure APTD mode
- ii. Simultaneous diffuse and filamentary regime: “hybrid mode”

In the following, the experimental results on the discharge characterisation for both modes will be separately described with respect to the N<sub>2</sub>O admixture and the underlying mechanisms will be analysed afterwards in combination with the modelling results in a conclusive section.

### 3.1 Pure APTD mode

The DBD in virtually pure N<sub>2</sub> in a 1 mm gap ignited at a voltage of 12.6 kV<sub>pp</sub> (4.5 kV<sub>RMS</sub>), featuring a diffuse, i.e. non-constricted, emission in the volume in front of the anode. An example of the discharge morphology is presented in Fig. 3 for 1 vol% N<sub>2</sub>O in N<sub>2</sub>, showing

<sup>1</sup> In the following, all excited species are written in abbreviated form to improve readability, e.g. N<sub>2</sub>(A<sup>3</sup> $\Sigma_u^+$ ) goes as N<sub>2</sub>(A).



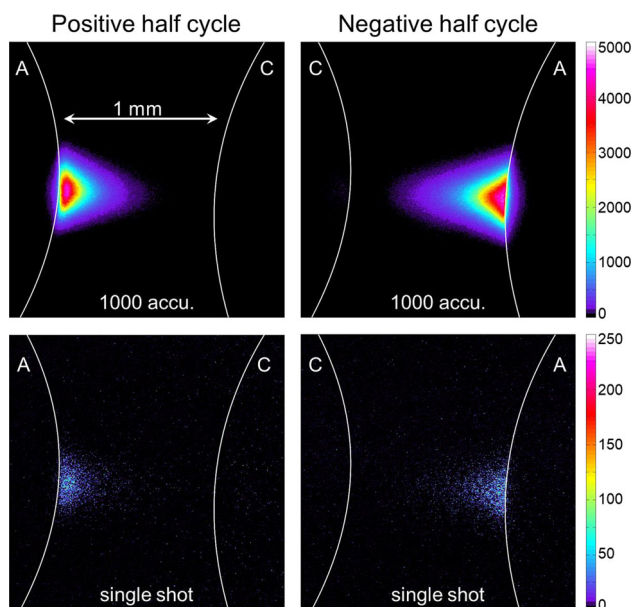


**Fig. 3** Discharge morphology of a sine-operated DBD with  $12.6\text{ kV}_{\text{pp}}$  at  $10\text{ kHz}$  and  $1\text{ vol}\%$   $\text{N}_2\text{O}$  in  $\text{N}_2$ . The surface of the half-spherical electrodes is indicated by white lines (A ... Anode, C ... Cathode). The left electrode is powered (A in pos. half cycle), the right electrode is grounded (A in neg. half cycle). Accumulation of 1000 HV cycles with an ICCD gate of  $10\ \mu\text{s}$  at the time of maximum emission (top row) and corresponding single shots with maximal gain of the ICCD (bottom row, i.e. intensity only row-wise comparable). The intensity is displayed in pseudo-colour with linear scaling

spectrally integrated ICCD images featuring 1000 accumulations and a single event with a  $10\ \mu\text{s}$  ICCD gate width. The ICCD recordings of single events clearly confirm the generation of a diffuse discharge (bottom row in Fig. 3), i.e. the diffuse appearance visible in the accumulated images is not caused by an overlapping of discharge events with different individual structures. The DBDs feature a triangle-shaped emission with its maximal diameter directly in front of the anode, which tapers within the gap towards the cathode. This diffuse emission structure in the gap was found for all  $\text{N}_2\text{O}$  admixtures<sup>2</sup> up to  $5\text{ vol}\%$  in  $\text{N}_2$  driven by a sinusoidal waveform with  $12.6\text{ kV}_{\text{pp}}$  (see Fig. 4), which was checked by single shots for each case (not shown). The emission diameter in front of the anode is decreasing with increasing  $\text{N}_2\text{O}$  content, from about  $0.8\text{ mm}$  for virtually pure  $\text{N}_2$  down to about  $0.3\text{ mm}$  for  $5\text{ vol}\%$ , while the emission intensity dropped significantly (note the comparable logarithmic intensity scale in Fig. 4).

For all  $\text{N}_2\text{O}$  concentrations, the discharge emission is increasing exponentially towards the anode, reaching its maximum just in front of the anode surface. This can be clearly seen in the emission profiles shown in Fig. 5, where the emission along the central axis of the gap is plotted for both half cycles. Electronic excita-

<sup>2</sup> No discharge could be ignited for  $10\text{ vol}\%$   $\text{N}_2\text{O}$  in  $\text{N}_2$  at  $12.6\text{ kV}_{\text{pp}}$ .

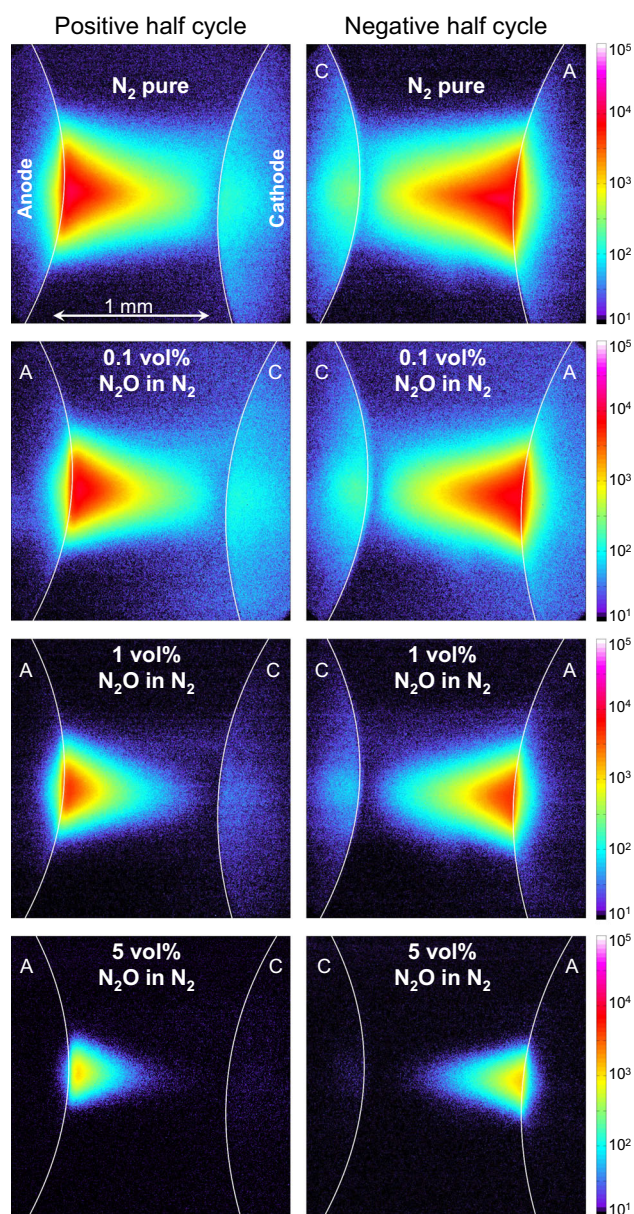


**Fig. 4** Discharge morphology at the maximum emission time window ( $10\ \mu\text{s}$  ICCD gate width corresponding to phase position (II) for the left column and (VII) for the right column (see Fig. 6)) for different gas mixtures at  $12.6\text{ kV}_{\text{pp}}$ . Each image is the result of 1000 accumulations. The intensity is colour-coded with a logarithmic scaling (comparable for all cases here)

tion of  $\text{N}_2$  (more precisely the second positive system of  $\text{N}_2(\text{C})$ ) is responsible for the major part of the emission of DBDs with a  $\text{N}_2$  admixture [23]. An exponentially increasing intensity towards the anode is a characteristic of a Townsend discharge, where no significant space charge is generated and consequently, the electron density is exponentially increasing towards the anode, too [32]. Thus, the applied electric field is not disturbed by space charges in the gap [33]. Comparing the maximum intensities near the anode for both half cycles in Fig. 5

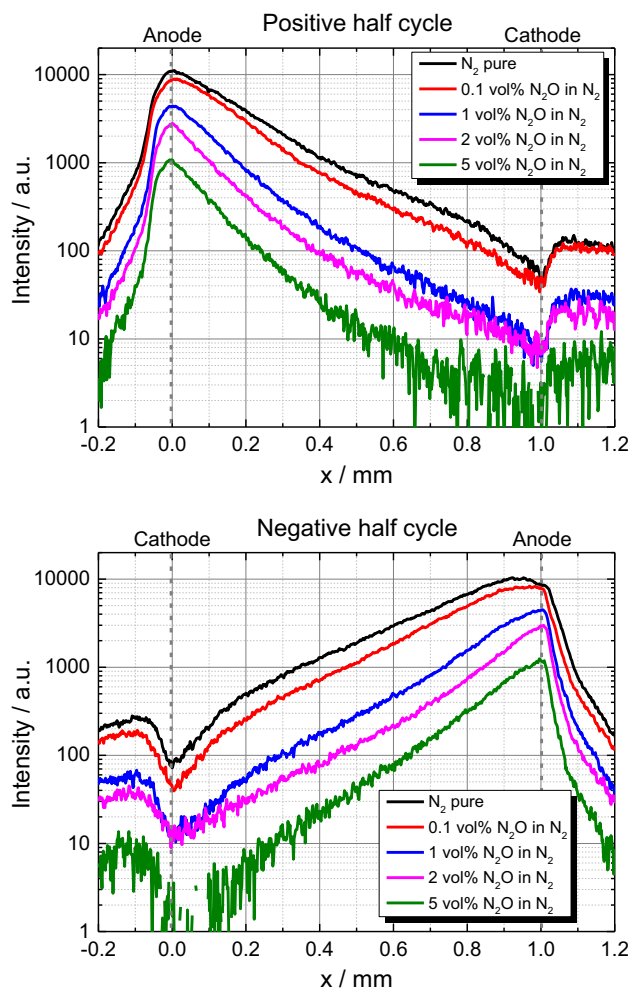


**Fig. 5** Axial intensity profiles along the gap axis in dependence on the gas composition at  $12.6 \text{ kV}_{\text{pp}}$  for both the positive and negative half cycle. The positions of (momentary) anode and cathode surfaces are indicated by grey dashed lines

for varying  $\text{N}_2\text{O}$  admixtures shows a decrease with rising  $\text{N}_2\text{O}$  content, resulting in an intensity reduction of about one order of magnitude for 5 vol%  $\text{N}_2\text{O}$  compared to virtually pure  $\text{N}_2$ . The same trend was found for a pulsed-operated single-filament DBD generated in these gas mixtures using the same arrangement [24].

The profiles for the positive and negative half cycles are almost symmetrical. Minor differences could be explained by slight anomalies in the electrode geometry (e.g. the shape of the dielectric). The re-increase of the signal on the momentary cathode (right of 1.0 mm or left of 0 mm, respectively) is most likely caused by a reflection of light at the cathode surface.

To track the temporal development of the diffuse DBD, 1000 accumulations with an ICCD gate width of  $10 \mu\text{s}$  were recorded phase-resolved over a complete HV period, shown exemplarily for virtually pure  $\text{N}_2$  in Fig. 6 (see corresponding numbers (I) to (X)). In the top row of Fig. 6, the applied HV waveform and the total current are shown (averaged over 1000 peri-

ods). The measured current mainly shows the displacement current  $I_{\text{dis}}$ , while the actual discharge current is hardly visible. From the displacement current, it is possible to calculate the total capacitance  $C_{\text{tot}}$  of the DBD arrangement according to the relation

$$I_{\text{dis}} = C_{\text{tot}} \frac{dU}{dt}$$

using the first time derivative of the applied voltage  $U$ . The value for  $C_{\text{tot}}$  was found to be approximately  $0.2 \text{ pF}$ , which is in good agreement with the total capacitance obtained for pulsed operation in the same arrangement [34]. The discharge current of the APTD can only be seen as minuscule “humps” on the sinusoidal curve (indicated by circles in the top row of Fig. 6). According to the literature, the maximum current density of an APTD is of the order of  $1 \text{ mA/cm}^2$  [35] or even lower [16, 22]. The diameter of the APTD in the arrangement under investigation is less than 1 mm (e.g. about a factor of 10 smaller than in [16]), which results in a maximal current of the order of  $1 \mu\text{A}$ , which is lower than the amplitude of the displacement current. Unfortunately, such low current signals can hardly be analysed with the available electrical diagnostics. Distinct current peaks, as they are typical for filaments, are not obtained at  $12.6 \text{ kV}_{\text{pp}}$  for all investigated  $\text{N}_2\text{-N}_2\text{O}$  gas mixtures (reminder: no discharge inception at  $12.6 \text{ kV}_{\text{pp}}$  for 10 vol%  $\text{N}_2\text{O}$ ). Nevertheless, the small deviations of the sine waveform from the displacement current can be used as an indication of discharge activity, as they correspond to maximal emission intensity (as described in what follows). The ICCD images in Fig. 6 show the discharge starting at the anode, gradually rising towards the discharge volume, and simultaneously expanding in the radial direction (see positions (I) to (III) and (VI) to (VII) in this figure). After reaching the maximum of the applied voltage, the emission intensity reduces with time and withdraws towards the anode (see positions (III) to (V) and (VIII) to (X) in Fig. 6). Such discharge development for an APTD in  $\text{N}_2$  is in agreement with the literature, e.g. [16, 36]. The emission in front of the cathode in figures (I) and (VI) is due to two different effects: first, the actual gap voltage is temporally ahead to the applied voltage; i.e. the voltage across the gap reaches the breakdown threshold value earlier than the applied voltage, see modelling results in Sect. 3.3 (Fig. 15 a). Second, the  $10 \mu\text{s}$  ICCD gate leads to additional accumulation of light from the preceding half cycle with opposite polarity (i.e. the actual transition from momentary anode to cathode and vice versa occurs before the applied HV changes its polarity, since the gap voltage is always slightly ahead of the applied HV in APTD [35]). The same spatio-temporal discharge emission development was found for all  $\text{N}_2\text{O}$  admixtures for  $12.6 \text{ kV}_{\text{pp}}$ , although the intensity and the axial extension of the emission in the gap was strongly decreased with increasing  $\text{N}_2\text{O}$  content. In the following section, the impact of increasing the HV amplitude on the DBD characteristics will be described



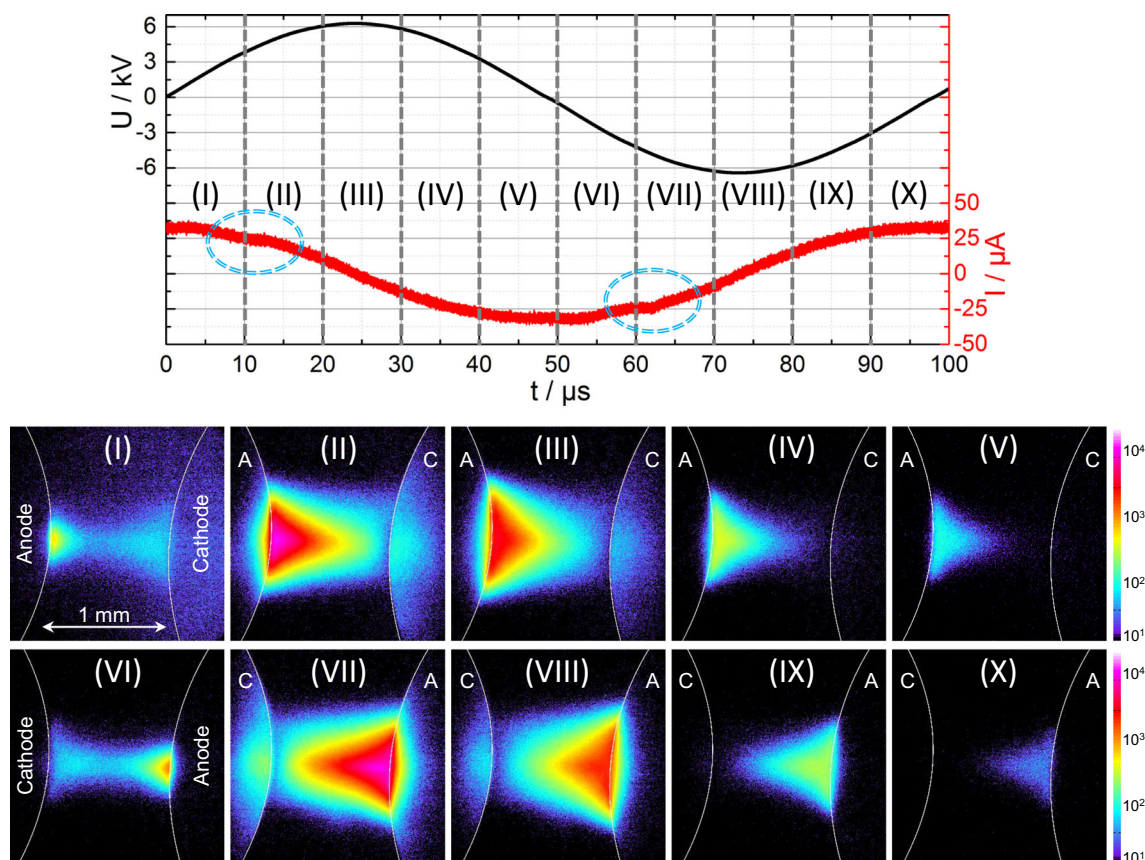


**Fig. 6** Discharge development of a sinusoidal-operated DBD at  $12.6 \text{ kV}_{\text{pp}}$  in virtually pure  $\text{N}_2$ . The top diagram shows the measured voltage waveform and the corresponding total current (averaged over 1000 HV periods). Phase-resolved ICCD images over the full period (1000 accumulations per image), as indicated by (I) to (X), are given in the bottom part of each sub-figure. The intensity is colour-coded with a logarithmic scaling and maximal intensity value of 32000 counts

for the same gas composition variation as presented in this paragraph.

### 3.2 Hybrid mode

A significant change in the discharge behaviour was found when the amplitude of the applied voltage is increased to  $14 \text{ kV}_{\text{pp}}$ , which was the maximum voltage of the available power supply. The APTD is interrupted by a periodic occurrence of filamentary breakdowns at the negative half cycle. This is visualised in Fig. 7, where 50 periods of the applied HV waveforms are exemplarily shown with the corresponding currents for virtually pure  $\text{N}_2$  and 1 vol%  $\text{N}_2\text{O}$  in  $\text{N}_2$ . For virtually pure  $\text{N}_2$ , these filaments occur fairly regularly every fifth period (i.e. with  $500 \mu\text{s}$  between them), while they appear every second period for 1 vol%  $\text{N}_2\text{O}$  in  $\text{N}_2$  (and also for 5 vol%  $\text{N}_2\text{O}$  in  $\text{N}_2$ , not shown). The reason for the appearance during the negative half cycle is likely due to a DC bias of about  $-130 \text{ V}$ , which is expected to cause asymmetric surface charge distributions influencing the electric field configuration in the gap. Unfortunately, the DC bias was an intrinsic and unavoidable feature of the used power supply.

In Fig. 8 a, the spatio-temporal discharge development for virtually pure  $\text{N}_2$  is shown for  $14 \text{ kV}_{\text{pp}}$  (phase-resolved featuring 1000 accumulation per  $10 \mu\text{s}$  time step analogous to Fig. 6). It has to be emphasised that the spatio-temporal discharge developments shown in Fig. 8 cannot distinguish between the intermediate filament and the diffuse APTD during the negative half cycle due to the accumulation. The discharge always operates as an APTD in the positive half cycle, which was checked by single-shot images using the same ICCD settings as described in Fig. 6. The emission intensity in the volume is higher and the discharge is wider than for  $12.6 \text{ kV}_{\text{pp}}$ , but the maximum of the emission is still occurring near the anode as expected for an APTD. The discharge starts to decay during the phases (III–V) shown in Fig. 8 a and an APTD with reverse polarity starts to develop after the voltage zero crossing. Since a filamentary discharge ignites only every fifth period during the negative half cycle of the applied HV, the negative current peak visible in time window (VI) features a much lower (absolute) value due to the averaging. The ICCD image in this time window (Fig. 8 (a) (VI)) shows a discharge channel connecting both electrodes and spreading on the surfaces, which is an overlay of the APTD and the filaments. The dis-

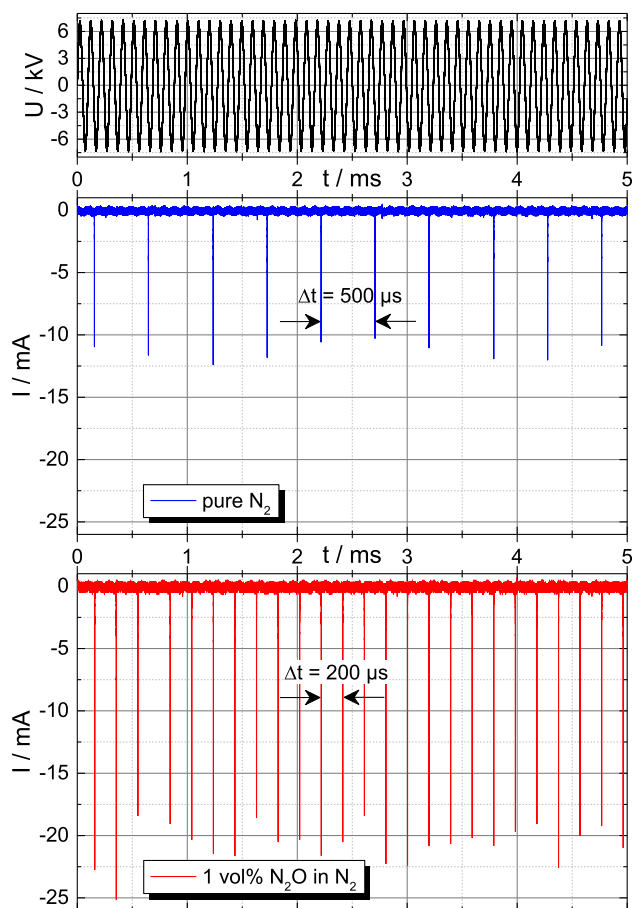


**Fig. 7** Applied voltage waveform (top row, 14 kV<sub>pp</sub>) and corresponding measured currents for virtually pure N<sub>2</sub> (middle row) and 1 vol% N<sub>2</sub>O in N<sub>2</sub> (bottom row) over 50 periods showing the periodical occurrence of filamentary discharges identifiable by distinct (in this case negative) current peaks

charge continues as an APTD with the emission maximum at the anode further decaying (see Fig. 8 (a) (VII–X)). Since both regimes, i.e. the filamentary and the APTD one, coexist, it is called “hybrid” regime<sup>3</sup> in the following.

A similar behaviour was observed for 1 vol% N<sub>2</sub>O in N<sub>2</sub> as shown in Fig. 8 b. The discharge is an APTD in the positive half cycle (Fig. 8 (b) (I–V)) and a filament is formed in the negative half cycle at around 60  $\mu s$ . The ICCD images in Fig. 8 (b) (VI–VII) clearly show a discharge channel, although this is also an overlay of the APTD and the filament, since the filamentary discharge occurs only every second period. Consequently, the averaged current peak of the filament is stronger, which is due to a combination of the higher (absolute) current and the more frequent occurrence of filaments

<sup>3</sup> What is called “hybrid regime” here differs from the “hybrid mode” defined by Boisvert et al. [14], where it is defined as an intermediate state between the atmospheric pressure Townsend and glow discharge (APTD and APGD, respectively), which are both diffuse, i.e. non-filamentary discharges.

for 1 vol% N<sub>2</sub>O in N<sub>2</sub> in comparison with the discharge in virtually pure N<sub>2</sub> (see Fig. 7). Since the emission intensity of a filamentary discharge is much higher compared to the intensity of a diffuse APTD, the channel is quite pronounced. While there is no emission in the gap during the negative half cycle after a filament occurrence, the discharge features again diffuse emission in front of the anode (see Fig. 8 (b) (VIII)).

In Fig. 9, the emission structure of the discharge during the maximal intensity at the positive and negative half cycle is shown for different N<sub>2</sub>O admixtures to N<sub>2</sub>. Generally, the emission intensity is decreasing with increasing N<sub>2</sub>O concentrations similar to the 12.6 kV<sub>pp</sub> case (note the logarithmically scaled intensity in Fig. 9). While the discharge is diffuse during the positive half cycle, with the APTD-typical emission maximum in front of the anode, the discharge at the negative half cycle is only in the diffuse APTD mode for 0.1 vol% N<sub>2</sub>O in N<sub>2</sub>. Due to the reduced emission and the more frequent occurrence of a filament for 1 and 5 vol% N<sub>2</sub>O admixtures compared to virtually pure N<sub>2</sub>, the filament appearance in the volume is more evident for 1 and 5 vol% N<sub>2</sub>O in N<sub>2</sub>.

To characterise the intermediate filaments, the discharge current for each filament was recorded. This was done by triggering the oscilloscope on a negative current value, which was explicitly higher than the displacement current<sup>4</sup> to ensure the recording of a distinct current peak, which are characteristic for filamentary DBDs [38,39]. In this context, it has to be emphasised that the discharge current peaks measured for these filaments in the hybrid mode are related to a streamer-like breakdown [40] and not to an atmospheric pressure glow discharge. In Fig. 10, the averaged current pulses are shown in a 150 ns time window (top) and with an enlargement on the initial current slope (12 ns, bottom). The current pulses of single recordings feature a very similar shape. For a better comparison, the current axis was inverted, and the current waveform for 10 vol% N<sub>2</sub>O in N<sub>2</sub> at 14 kV<sub>pp</sub> was added, i.e. for a filamentary DBD at both half cycles. However, it has to be noted that more than one filament per half cycle can be obtained at these conditions and these filaments are not well-localised as in the case of the hybrid regime.

The current of the filaments significantly depends on the gas composition as also described for pulsed operation [24]. The current pulse amplitude increases from about 10 mA to 100 mA with increasing N<sub>2</sub>O admixture, while the duration of the current flow is higher for lower N<sub>2</sub>O concentrations and the current decays fastest for the highest N<sub>2</sub>O concentration. It can be clearly seen that the current slope is getting steeper with rising N<sub>2</sub>O concentration. Furthermore, it is possible to calculate the transferred charge per filament  $Q$  by integrating the current waveforms over time. The results are shown in Fig. 11. Due to the longer duration of the discharge, the highest amount of charge (about

<sup>4</sup> Unfortunately, it was also for 14 kV<sub>pp</sub> applied HV not possible to properly measure the discharge current during the APTD phase due to the still too low current amplitude.

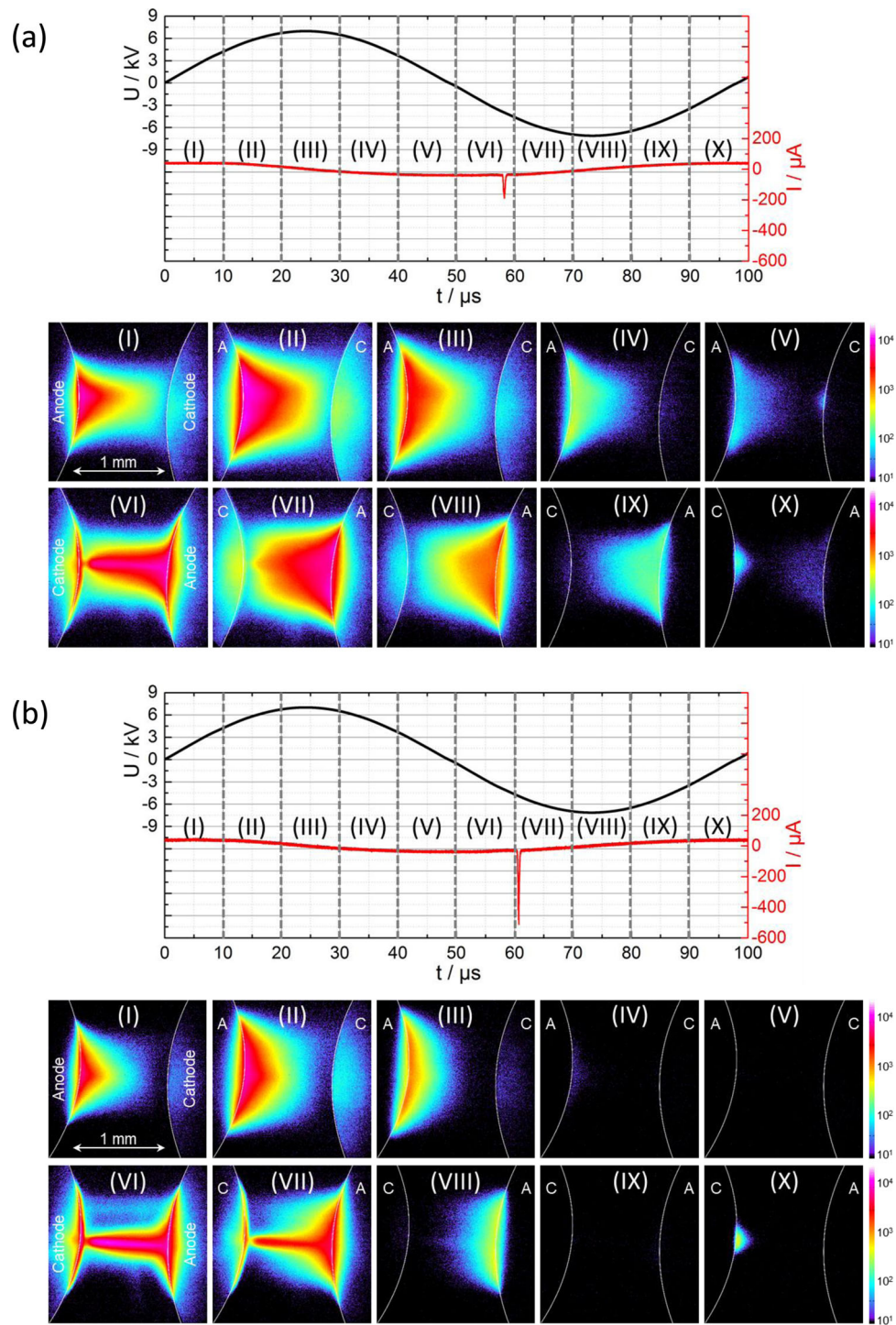


**Fig. 8** Discharge development of a sinusoidal-operated single DBD at  $14.0 \text{ kV}_{\text{pp}}$  in virtually pure  $\text{N}_2$  **a** and with 1 vol% admixture of  $\text{N}_2\text{O}$  in  $\text{N}_2$  **b**. The top diagram shows the measured voltage waveform and the corresponding total current (averaged over 1000 HV periods). Phase-resolved ICCD images over the full period (1000 accumulations per image), as indicated by (I) to (X), are given in the bottom part of each sub-figure. The intensity is colour-coded with a logarithmic scaling and maximal intensity value of 32000 counts



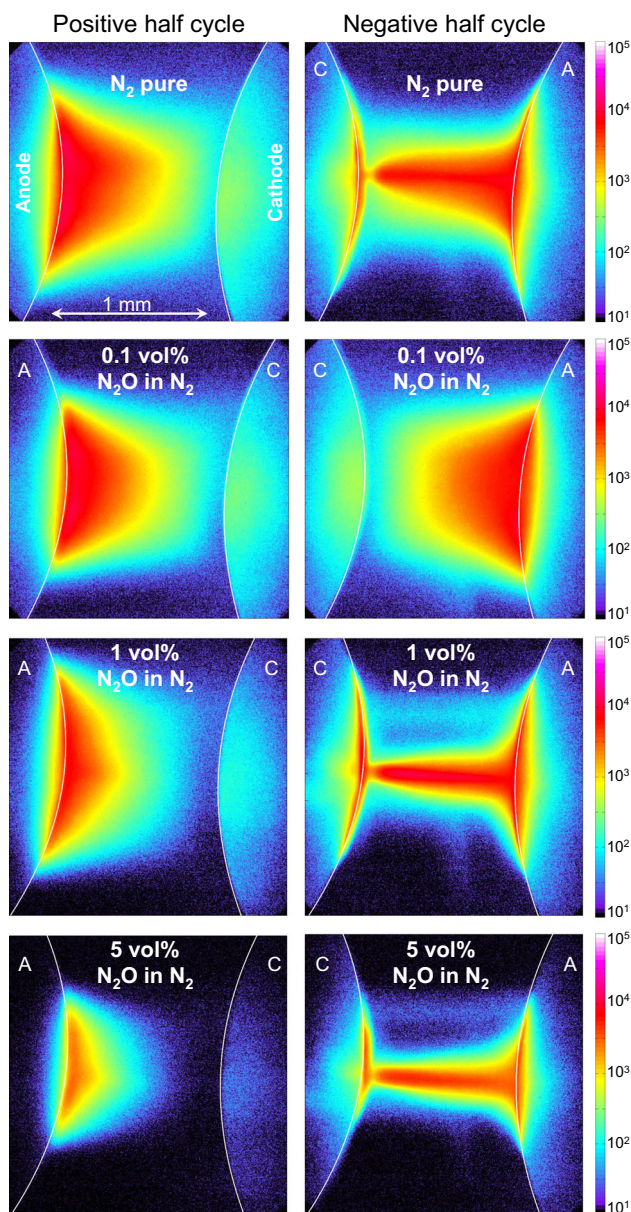


**Fig. 9** Discharge morphology at the intensity maximum in dependence on the  $N_2O$  admixture at  $14\text{ kV}_{pp}$  for positive and negative half cycles. Each image is the result of 1000 accumulations. The intensity is logarithmically scaled in pseudocolour

$0.45\text{ nC}$ ) is dissipated in the case of no  $N_2O$  admixture, although the current peak is lowest in this case. The higher the admixture of  $N_2O$ , the lower the charge per filament in the hybrid regime (down to about  $0.23\text{ nC}$  for  $5\text{ vol}\% N_2O$ ). In the case of  $10\text{ vol}\% N_2O$  concentration, i.e. filamentary case in both half cycles, the discharge features a much higher current peak and the charge increases again to about  $0.3\text{ nC}$ , although the current decays much faster compared to all other investigated  $N_2O$  admixtures similar to the pulsed operation [24] (although the peak current here is about four times lower compared to pulsed operation).

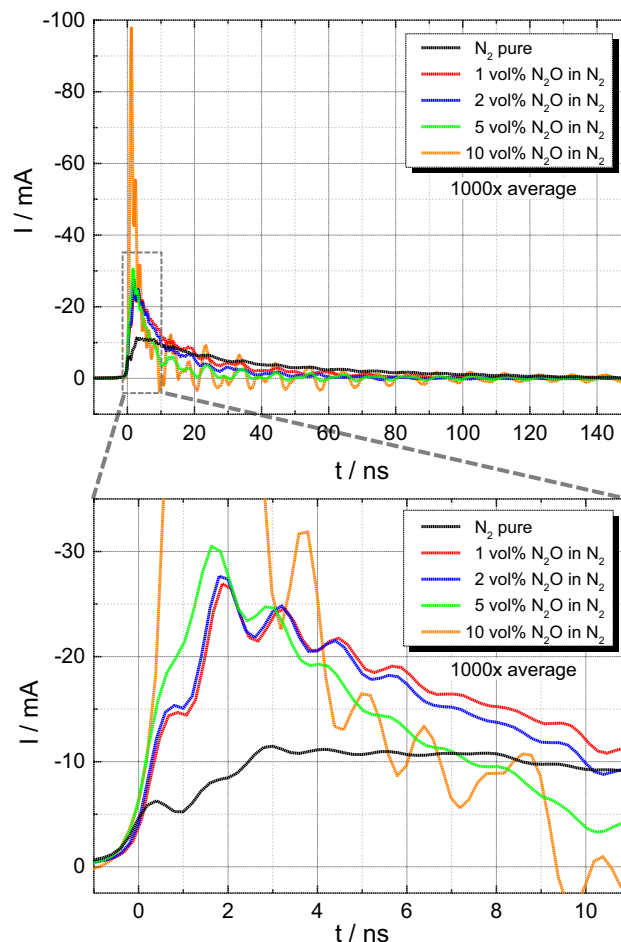


**Fig. 10** Discharge current for the filamentary case as a function of the  $N_2O$  concentration for  $14\text{ kV}_{pp}$ . The results are averaged over 1000 individual filaments (triggered on the current, i.e. not synchronised with the applied HV). Single shots of the current (not shown) feature a very similar pulse shape

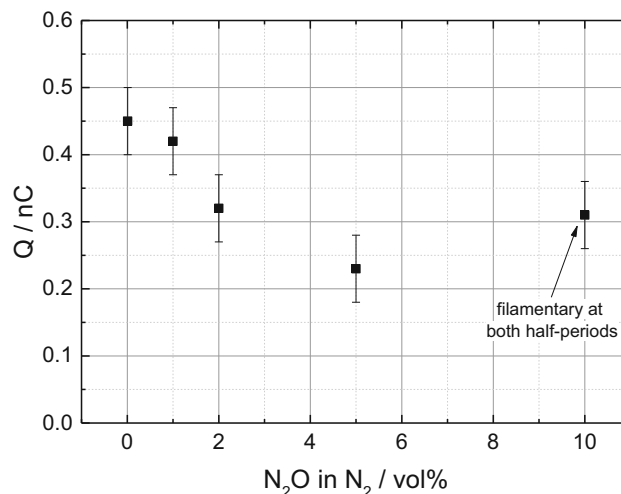


**Fig. 11** Dissipated charge per filamentary discharge for the different gas compositions

It has to be noted that the filamentary discharge for the case of virtually pure  $N_2$  occurs only every fifth period compared to about every second period for the higher  $N_2O$  admixtures, i.e. the time-averaged charge transferred by filaments is about two times higher for 1 vol%  $N_2O$  in  $N_2$  (although  $Q$  is slightly lower for 1 vol%  $N_2O$ ), and about the same for 5 vol%  $N_2O$  in  $N_2$  compared to  $N_2$ .

In addition to the electrical characterisation of the filaments, ICCD images of individual filamentary discharges and their spatio-temporal development by jitter-corrected streak images were obtained. They are displayed in Fig. 12 for virtually pure  $N_2$  as well as 1 and 2 vol%  $N_2O$  in  $N_2$ . The ICCD images of the individual discharges using  $10\ \mu s$  ICCD gate show a constricted channel in the volume and spreading surface discharge channels both on the anode and the cathode. For virtually pure  $N_2$  the channel in the volume is about  $200\ \mu m$  in diameter and features an intensity maximum near the cathode (see Fig. 12 a (left)). The channel diameter is about  $100\ \mu m$  both for 1 and 2 vol%  $N_2O$  in  $N_2$ , while the emission maximum is also near the cathode (see Fig. 12 (b,c) (left)). The spatio-temporal discharge development recorded by the streak camera is characterised by a cathode-directed streamer followed by a transient glow-like phase for all gas compositions, where filaments occur. Generally, a higher  $N_2O$  admixture decreases the discharge emission duration. However, there are differences concerning the discharge inception, e.g. the streamer inception point in the gap is shifted away from the cathode for higher  $N_2O$  admixtures while the maximal streamer propagation velocity roughly triples (from  $\approx 2 \times 10^5$  to  $6 \times 10^5$  m/s). For pure  $N_2$  the streamer starts about  $200\ \mu m$  in front of the cathode; for 1 and 2 vol%  $N_2O$  it starts nearly in the middle of the gap at about  $450\ \mu m$  in front of the anode. A similar effect was reported for filamentary, pulsed-operated DBDs in a similar single-filament configuration, which was related to elevated pre-ionisation in the gap, i.e. the higher the pre-ionisation the slower the streamer and the shorter its starting distance to the cathode [26]. Furthermore, this is in accordance with the measurements of the discharge current during the filamentary discharges (see Fig. 10), i.e. the current slope is much smoother for virtually pure  $N_2$  compared to 1 and 2 vol%  $N_2O$  in  $N_2$  (for which the slopes as well as the streamer propagation velocities are nearly the same). Therefore, these similarities are a strong indication that these filaments are igniting in a highly pre-ionised gap [41], although it is important to note that also the gas composition has a distinct impact on the streamer inception [24, 42]. In addition, for the virtually pure  $N_2$  case, it seems that after the short cathode-directed streamer a slower anode-directed ionisation front starts propagating, which was also found to be a breakdown regime for highly pre-ionised single-filament DBDs [26, 43].

Using the streak camera it is possible to record the discharge emission over an entire single HV period, as shown in Fig. 13 for  $14.0\ kV_{pp}$  in virtually pure  $N_2$ . Displayed are single shots and images of 100 accumu-

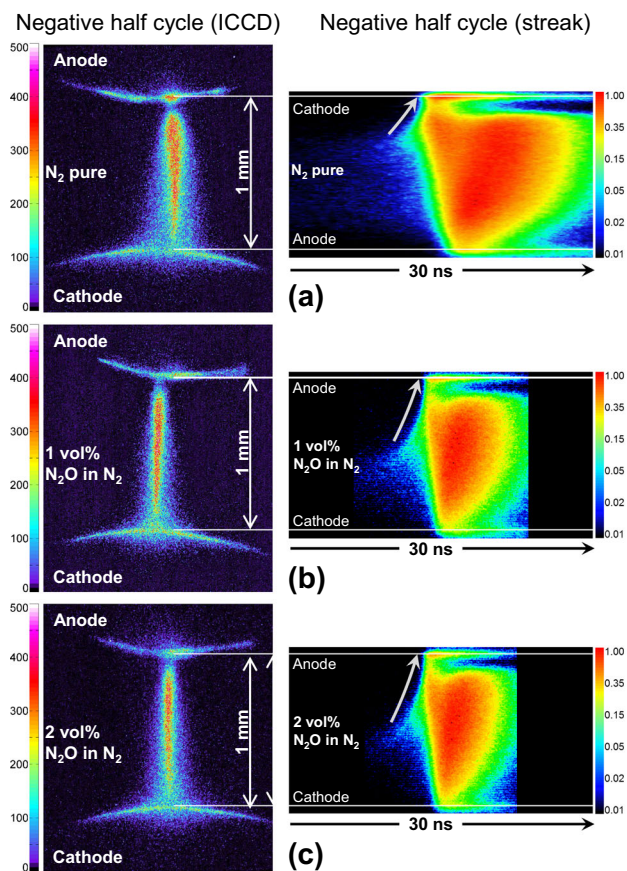


**Fig. 12** ICCD images (left) and streak recordings (right) of filaments in **a** pure  $N_2$ , **b**  $N_2$  with 1 vol%  $N_2O$ , and **c**  $N_2$  with 2 vol%  $N_2O$  for  $14\ kV_{pp}$ . While the ICCD images are for an individual discharge event ( $10\ \mu s$  ICCD gate width, maximal ICCD gain), the streak images are compiled of 300 microdischarges, using the jitter correction function of the streak camera software [37]. The intensity is in pseudo-colour, for the ICCD images with a linear and for the streak images with a logarithmic scaling

lated events for the hybrid mode and the APTD mode for both half cycles in a  $100\ \mu s$  time window. The filament is much more intense than the APTD and covers almost the entire gap distance (note the logarithmic intensity scale in Fig. 13 with respect to the maximal intensity of the filament). Furthermore, the filament intensity is maximal in the gap volume near to the cathode, while the emission of the APTD concentrates near the anode surface. Even though the temporal resolution of the streak images shown in Fig. 13 is only of the order of  $1\ \mu s$ , it can without doubt be stated that the APTDs last much longer than the filamentary ones as also visible from the phase-resolved ICCD images (see Fig. 8). Additionally, the inception of the APTD during the positive half cycle evolves at a lower applied voltage when a filament occurred in the previous negative half cycle. Although, the impact of the filament on the gap voltage has to be considered, it is clear that there is a distinct shift in the discharge inception after the occurrence of a filament. This can be further analysed by



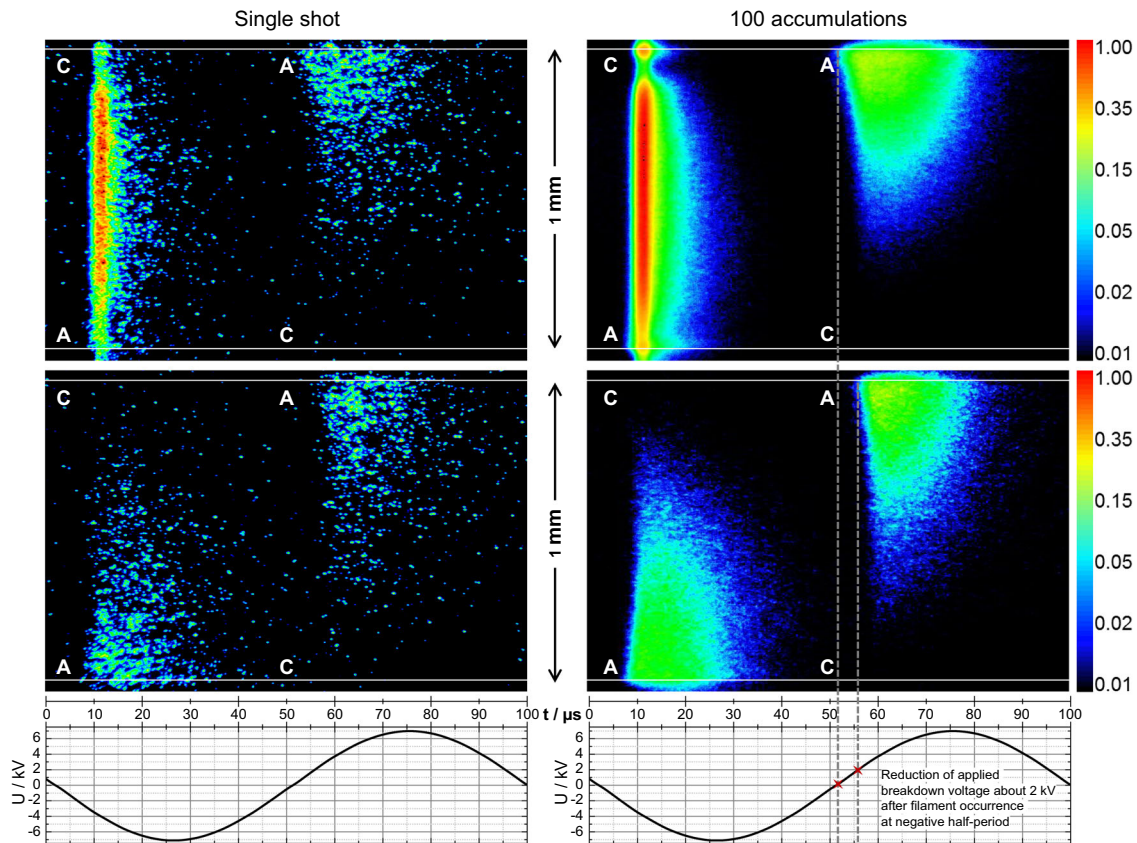


**Fig. 13** Voltage curves and streak images (single shots and 100 accumulations) over the full cycle of discharges operated with  $14.0\text{ kV}_{\text{pp}}$  in pure  $\text{N}_2$ . Top: cycles with hybrid mode (filament and APTD); middle: APTD mode in both half cycles; bottom: voltage curves. The high voltage is applied to the top electrode and the values of discharge inception for both cases are marked. The intensity is colour-coded with logarithmic scaling with respect to the maximum in the top left image

comparing emission profiles from streak recordings like shown in Fig. 13, which were spatially averaged over the entire discharge gap. Figure 14 shows temporal emission profiles for different gas mixtures. For the APTD mode shown for virtually pure  $\text{N}_2$ , 1 and 2 vol%  $\text{N}_2\text{O}$  admixture in Fig. 13 a similar profiles are obtained in both half cycles. For pure  $\text{N}_2$  the emission between the two cycles does not vanish to zero, i.e. there is significant emission during the complete HV period. Increasing the  $\text{N}_2\text{O}$  admixture to  $\text{N}_2$ , the emission per half cycle gets shorter, weaker and decays faster.

In the following subsection, the experimental findings presented in Sects. 3.1 and 3.2 will be explained by identifying the dominant processes and mechanisms responsible for the occurrence and transition between the APTD and filamentary mode.

### 3.3 Fluid modelling results and discussion

Analysis and interpretation of the measured data are supported by numerical simulations using the 1D fluid-Poisson model described in Sect. 2.2. Model calculations were performed for the experimental condition using a voltage of  $12.6\text{ kV}_{\text{pp}}$  and a gas mixture of 0.1 vol%  $\text{N}_2\text{O}$  in  $\text{N}_2$  (assuming an  $\text{O}_2$  impurity of 30 ppm). For these

conditions, a diffuse discharge in the APTD regime is observed experimentally and predicted by the simulations. It is important to note that the 1D model used in the present study is not capable of resolving the radial discharge dynamics and filament formation, which plays an important role at higher applied voltages where the hybrid discharge mode was observed experimentally. Furthermore, the chemistry of long-living heavy particle species and the formation of larger molecules occur on much longer time scales than the actual discharge activity. Hence, the spatially resolved fluid model including all relevant collision processes provides detailed insights into the initial discharge phase and is used here to analyse the transition of an initially high-current discharge mode to the APTD regime. Here it is important to note that the mode transition and the quasi-periodic results for the APTD regime are not influenced by the initial conditions used for the model calculations.

Figure 15 shows results of the model calculations for the time range from 300 to  $500\ \mu\text{s}$  corresponding to the end of the third (at  $t = 300\ \mu\text{s}$ ) to the beginning of the fifth (at  $t = 400\ \mu\text{s}$ ) period. This time range corresponds to the transition phase from the filamentary to the APTD regime. Note that the overall discharge behaviour during the following cycles remains the same, even though long-living species, such as atomic oxy-



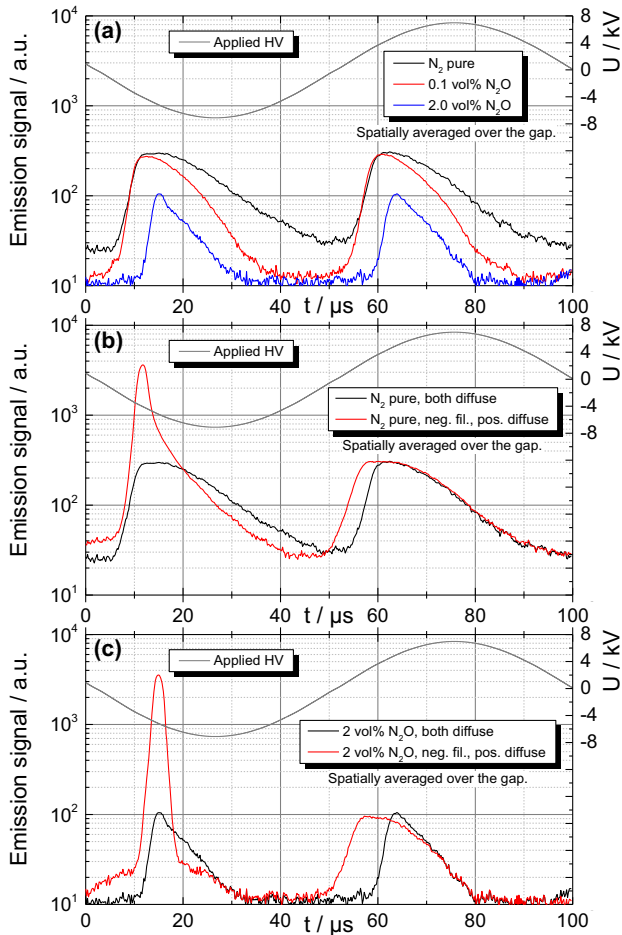


**Fig. 14** Temporally resolved emission profiles derived from the spatial average over the discharge gap in the streak images (14.0 kV<sub>pp</sub>). **a** Profiles for APTD cycles with different gas compositions; **b** profiles from hybrid cycles with a filament in the negative half cycle compared with the APTD cycles in pure N<sub>2</sub>; **c** same as (b), but for 2 vol% N<sub>2</sub>O in N<sub>2</sub>

gen, are not yet in quasi-periodic state. In Fig. 15 a, the applied voltage, the gas gap voltage, and the corresponding current density are displayed. The step and intense current density peak connected to a filamentary discharge during the positive half cycle at about  $t = 305 \mu\text{s}$  is deliberately truncated to show the details of the transition to the APTD mode within the subsequent two half cycles. This transition can be identified by the constant gap voltage during the current pulse—in contrast to the sharp dip in the gap voltage for the filamentary discharge—and the significant decrease of the current density to values below  $4 \text{ mA/cm}^2$ . Having in mind that the diameter of the measured discharge emission<sup>5</sup> for 0.1 vol% N<sub>2</sub>O in N<sub>2</sub> is about 0.5 mm at 12.6 kV<sub>pp</sub> (see Fig. 4), the maximal discharge current would be below  $10 \mu\text{A}$ , which is hardly measurable with the used current probe. After the transition to the

<sup>5</sup> Assuming this is a reasonable estimate for the region, where discharge current flows.

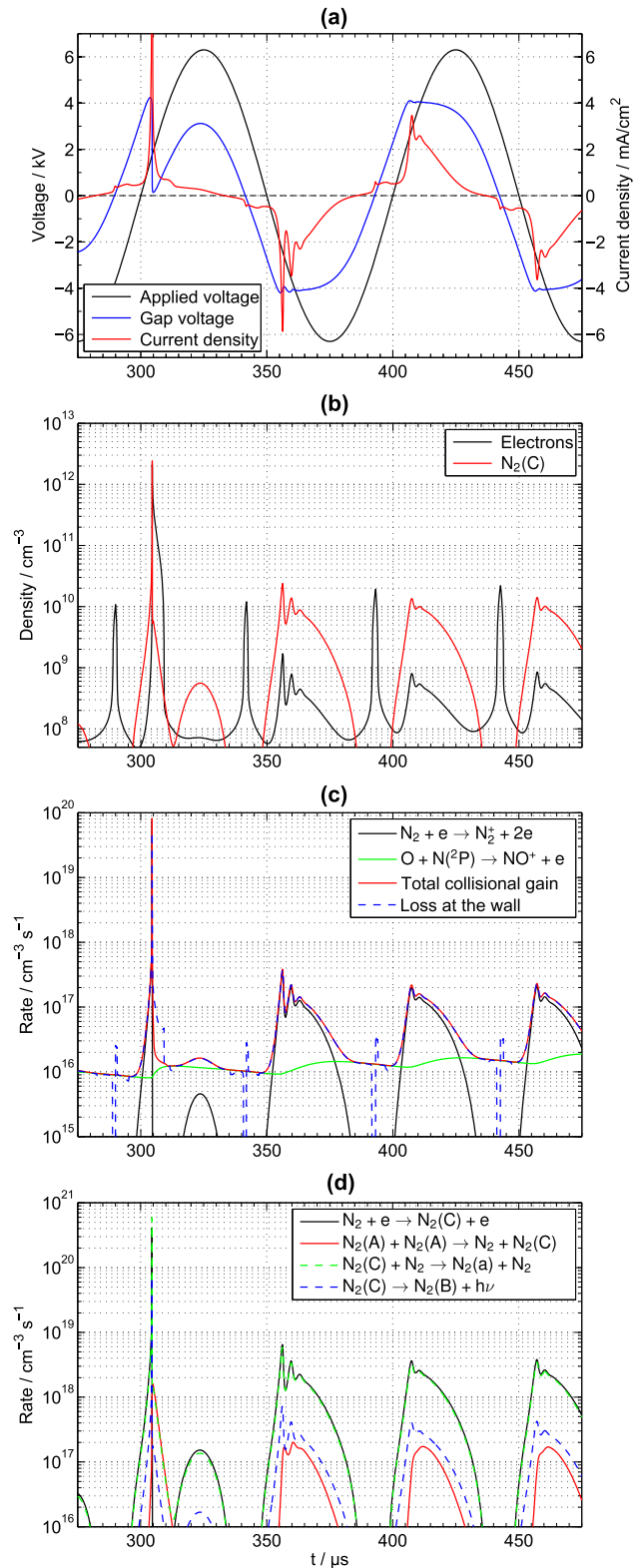
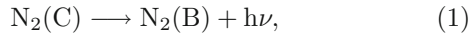


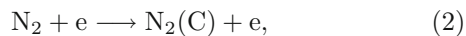
**Fig. 15** Modelling results for a sinusoidal-operated DBD with 12.6 kV<sub>pp</sub> at 10 kHz and 0.1 vol% N<sub>2</sub>O in N<sub>2</sub> showing the initial transition from filamentary to APTD regime. **a** applied voltage, gap voltage, current density; **b** spatially averaged density of electrons and N<sub>2</sub>(C) molecules; **c, d** spatially averaged rates of dominant gain (solid lines) and loss (dashed lines) processes for electrons and N<sub>2</sub>(C) molecules

APTD region, both the gap voltage and the current density become symmetric and quasi-periodic within a few periods.

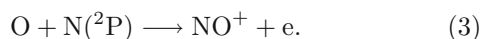
Figure 15 b shows the temporal development of the spatially averaged electron density and  $N_2(C)$  density during the mode transition. It can be clearly seen that these densities increase more rapidly to a much higher maximum value during the initial filamentary discharges and decrease more rapidly compared to the APTD phase. Note that the  $N_2(C)$  state is responsible for the major part of the emission, more precisely its electronic transition



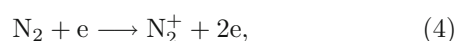
which is the so-called second positive system of  $N_2$  [23], i.e. the temporal evolution of the  $N_2(C)$  density corresponds to the temporal development of the emission in the gap. Comparing the  $N_2(C)$  density development from Fig. 15 b with the measured emission profile for 0.1 vol%  $N_2O$  concentration in Fig. 14 a shows a fair qualitative agreement. Since  $N_2(C)$  is mainly produced by direct excitation of  $N_2$  in collisions with electrons:



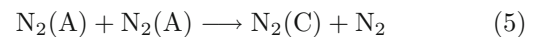
the electron density profile during the active APTD phase features a similar shape as the  $N_2(C)$  profile. However, the maximum of the electron density is located in between active diffuse discharge phases and corresponds to the zero crossing of the gap voltage, see Fig. 15 a. Therefore, it is directly connected to the polarity change of the discharge current and the related current jump observed in APTD [21]. At this instant, a reversal of the electric field in front of the momentary anode just before the polarity change of the gap voltage induces the transport of electrons towards the plasma bulk region, i.e. an ionisation front is moving from the momentary anode towards the momentary cathode. Figure 15 c shows that the ionisation during this time range and the resulting characteristic peak of the electron density is caused by the associative ionisation reaction



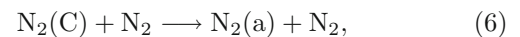
This is in accordance with the hypothesis provided by Tyl et al. [21] for the origin of the volume memory effect in atmospheric pressure DBDs in nitrogen with oxygen or nitric oxide additions. The often mentioned strong impact of the metastable  $N_2(A)$  by secondary electron emission from the dielectric surfaces was found to be of minor importance for occurrence of the APTD regime under given conditions, if the  $N_2O$  concentration exceeded 30 ppm. During the active APTD phase as well as the filamentary phase the electron multiplication is instead driven by the direct ionisation process



see (Fig. 15 c). Here it can be seen that this electron gain is mostly compensated by transport losses of electrons moving to the anode. The peaks and sinks of this loss process in between the active discharge phases correspond to the exchange of anode and cathode caused by the polarity change of the gap voltage (compare Fig. 15 (a and c) and the local reversal of the electric field. Moreover, the spatially averaged rates of dominant gain and loss processes for  $N_2(C)$  are given in Fig. 15 d, where solid lines indicate the gain and dashed lines the loss processes. While the direct electron impact excitation (reaction (2)) is the main production process for  $N_2(C)$ , the pooling reaction

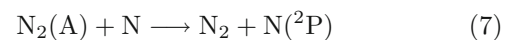


plays only a minor role. The major loss of  $N_2(C)$  is due to the collisional quenching process

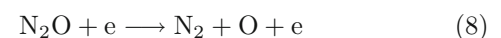


and partly by the spontaneous transition of  $N_2(C)$  to  $N_2(B)$  (reaction (2)), which is responsible for the major part of the optical emission.

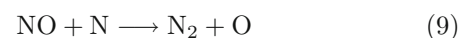
The importance of the associative ionisation process (3) for formation of the APTD mode requires a further study of the involved species, which are atomic oxygen in the ground state O, excited atomic nitrogen  $N(^2P)$  and, indirectly, metastable nitrogen  $N_2(A)$ . The spatially averaged densities and dominant gain/loss rates of these species are shown over time in Fig. 16. The density developments of metastable  $N_2(A)$  and excited  $N(^2P)$  species quickly become periodic in the filamentary and APTD regime, i.e. their densities are strongly modulated by the gas gap voltage reaching a mean value above  $10^{13} \text{ cm}^{-3}$ . In contrast, the density of oxygen atoms steadily builds up over multiple periods to about  $10^{15} \text{ cm}^{-3}$  and is not modulated by the varying HV waveform (see Fig. 16 a). The production of  $N(^2P)$  mainly occurs in the two-body energy transfer process



as shown in Fig. 16 b in agreement with [3]. Collisions of  $N(^2P)$  with NO lead to the re-generation of  $N_2(A)$  and also to the dissociation of NO, which slightly contributes to the production of atomic oxygen. However, the larger amount of atomic oxygen is produced from dissociation of  $N_2O$  in electron collisions



(dominant process in filamentary regime) and from the two-body energy transfer process



involving NO and nitrogen atoms in the ground state (dominant process in APTD regime), which is represented in Fig. 16 c. Note that NO is mostly generated

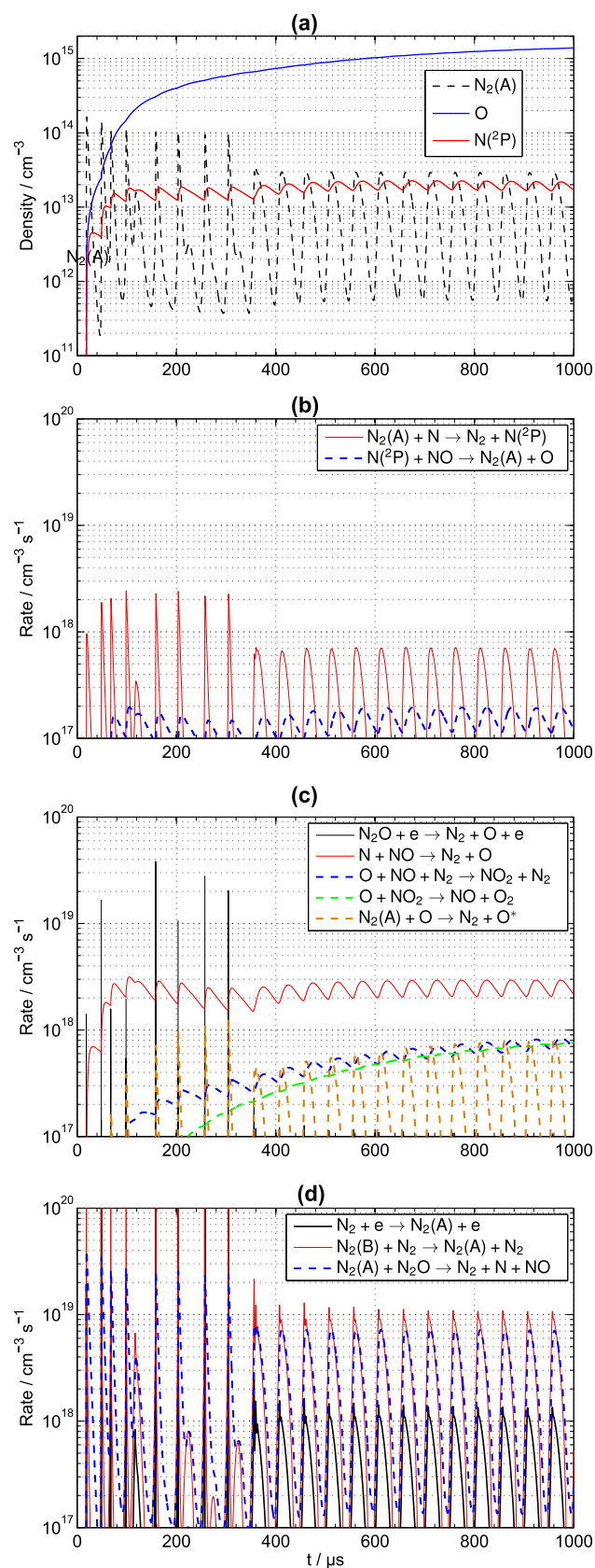
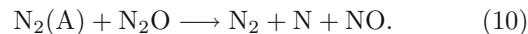


**Fig. 16** Spatially averaged densities **a** and dominant gain/loss rates (**b–d**) of  $\text{N}(\text{2P})$ ,  $\text{O}$  and  $\text{N}_2(\text{A})$  for the conditions of previous figures. Transition from filamentary to APTD regime occurs after  $300 \mu\text{s}$

by the following dissociative quenching process involving  $\text{N}_2\text{O}$  and  $\text{N}_2(\text{A})$ :



That is, metastable nitrogen  $\text{N}_2(\text{A})$  does not contribute significantly to the occurrence of an APTD here by means of secondary electron emission, but it is still very significant for the formation of the memory effect via the corresponding collision processes. Figure 16 d shows that  $\text{N}_2(\text{A})$  is predominantly generated from  $\text{N}_2(\text{B})$  via the process



while direct excitation of nitrogen molecules by electron collisions plays only a minor role. The modelling results also confirm that  $\text{N}_2(\text{A})$  is efficiently quenched by collisions with  $\text{N}_2\text{O}$ , where the reaction (10) represents the dominant loss process for  $\text{N}_2(\text{A})$ . Due to this fast quenching process, no significant amount of metastable nitrogen is present in between the active APTD phases as soon as elevated amounts of  $\text{N}_2\text{O}$  are mixed to  $\text{N}_2$ . For virtually pure  $\text{N}_2$  or very low  $\text{N}_2\text{O}$  admixtures, however, the larger concentration of  $\text{N}_2(\text{A})$  remains between individual discharges, which means that a significant  $\text{N}_2(\text{C})$  density is also generated in between the active APTD phases by the pooling reaction (5). This explains the emission in the gap during the complete HV period for virtually pure  $\text{N}_2$ , see e.g. Figs. 6 and 14 a.

In conclusion, the addition of  $\text{N}_2\text{O}$  to the nitrogen oxygen gas mixture, on the one hand, reduces the amount of metastable nitrogen, which is an important factor for transition to the APTD regime via secondary electron emission or the generation of excited nitrogen atoms via reaction (7). On the other hand, higher amounts of  $\text{N}_2\text{O}$  also provide an additional source of atomic oxygen and atomic nitrogen via reactions (8) and (10), respectively. This could also be the reason for the ability to generate a diffuse APTD up to 5 vol%  $\text{N}_2\text{O}$  in  $\text{N}_2$ , which was found in the experimental study. The reported intermediate occurrence of a filament could therefore be connected to a depletion of atomic oxygen and atomic nitrogen species. This is mostly also the reason for the more-frequent occurrence of filaments for 1 vol%  $\text{N}_2\text{O}$  in  $\text{N}_2$  compared to virtually pure  $\text{N}_2$  (see Fig. 7). Furthermore, dissociative attachment of electrons to  $\text{N}_2\text{O}$  becomes dominant at higher  $\text{N}_2\text{O}$  concentrations [24, 44] and the loss of electrons is compensated by the filamentary discharges, which then “feeds” the insufficient  $\text{O}$  and  $\text{N}(\text{2P})$  densities to continue the APTD mode in the subsequent HV half cycle. Possible mechanisms of  $\text{N}$  and  $\text{O}$  depletion include the sticking of these species at the wall and the loss due to the gas flow. The loss due to the gas expansion related to heating of the discharge is not expected to play a major role for the low-current APTD under consideration.



## 4 Summary

The impact of a N<sub>2</sub>O admixture to N<sub>2</sub> on a sine-driven DBD in a single-filament arrangement was studied experimentally and by 1D fluid modelling. It was found that at an applied voltage of 12.6 kV<sub>pp</sub> at 10 kHz a diffuse atmospheric pressure Townsend discharge (APTD) could be generated in a 1 mm gap up to 5 vol% N<sub>2</sub>O in N<sub>2</sub> on both the positive and negative half cycle. For 14 kV<sub>pp</sub> applied HV, an APTD is generated only for 0.1 vol% N<sub>2</sub>O in N<sub>2</sub> on both HV half cycles. For virtually pure N<sub>2</sub> and N<sub>2</sub>O concentrations up to 5 vol% the APTD mode is overlaid by an intermediate filament occurrence during the negative half cycle. This asymmetry is most likely induced by a slight negative DC bias of the HV supply, but however enabled the study of the interaction between filamentary and diffuse DBD modes. For 10 vol% N<sub>2</sub>O in N<sub>2</sub>, the DBD is in the full filamentary regime, i.e. it features constricted channels accompanied by steep current pulses on both HV periods. When a filament intermediately occurs during a negative half cycle, it directly effects the subsequent APTD, i.e. the filamentary breakdown leads to a transition back to the APTD mode causing earlier inception and longer emission duration.

The applied 1D fluid model was used to analyse the underlying reaction mechanisms. The obtained results confirm that for N<sub>2</sub>O containing N<sub>2</sub> the associative ionisation process  $O + N(^2P) \rightarrow NO^+ + e$  is the major electron source sustaining the volume memory effect and therefore the reason for the formation of a diffuse APTD. The dissociation of N<sub>2</sub>O by electron collisions and heavy-particle quenching processes provides an additional source of atomic oxygen and atomic nitrogen, which enables the occurrence of an APTD up to 5 vol% of N<sub>2</sub>O admixture by sustaining the above-mentioned associative ionisation. This means that under certain conditions also higher amounts of quenching species can be admixed to the working gas of DBDs for applications, where a diffuse mode is favourable.

Future investigations will include the implementation of a 2D model to properly describe the intermediate filamentary breakdown and the transfer of these results to larger DBD arrangements.

**Acknowledgements** This work was partly supported by the DFG-ANR project REDBIRD (DFG project number 316877802, ANR-16-CE92-0021) and the DFG project MAID (project number 466331904). The authors would like to thank A. Destrieux (currently affiliated with Université Laval, Canada) for supporting the measurements, U. Nehmzow (glassblower, INP) for manufacturing the discharge cell, and D. Loffhagen (INP) for providing electron transport and rate coefficients for the model and for fruitful discussions.

## Author contributions

HH and MK conducted the measurements and the data analysis, MMB performed the modelling and related data analysis. HH, MK, MMB and RB mainly wrote the manuscript; HH, MK, MMB, SD, NN, RB, and KDW were involved in the discussion and interpretation of the results and the conclusions.

**Funding Information** Open Access funding enabled and organized by Projekt DEAL.

**Data Availability Statement** This manuscript has associated data in a data repository. [Authors' comment: The datasets generated during the current study are available in the INPTDAT repository, <https://doi.org/10.34711/inptdat.667>.]

**Open Access** This article is licensed under a Creative Commons Attribution 4.0 International License, which permits use, sharing, adaptation, distribution and reproduction in any medium or format, as long as you give appropriate credit to the original author(s) and the source, provide a link to the Creative Commons licence, and indicate if changes were made. The images or other third party material in this article are included in the article's Creative Commons licence, unless indicated otherwise in a credit line to the material. If material is not included in the article's Creative Commons licence and your intended use is not permitted by statutory regulation or exceeds the permitted use, you will need to obtain permission directly from the copyright holder. To view a copy of this licence, visit <http://creativecommons.org/licenses/by/4.0/>.

## References

1. K.H. Becker, U. Kogelschatz, K.H. Schoenbach, R.J. Barker, *Non-equilibrium air plasmas at atmospheric pressure* (IoP Publishing, Bristol, Philadelphia, 2005)
2. K.H. Becker, K.H. Schoenbach, J.G. Eden, TOPICAL REVIEW: Microplasmas and applications. *J. Phys. D: Appl. Phys.* **39**, 55 (2006). <https://doi.org/10.1088/0022-3727/39/3/R01>
3. K.H. Becker, N.M. Masoud, K.E. Martus, K.H. Schoenbach, Electron-driven processes in high-pressure plasmas. *Eur. Phys. J. D* **35**(2), 279–297 (2005). <https://doi.org/10.1140/epjd/e2005-00199-0>
4. U. Kogelschatz, Filamentary, patterned, and diffuse barrier discharges. *IEEE Trans. Plasma Sci.* **30**, 1400–1408 (2002). <https://doi.org/10.1109/TPS.2002.804201>
5. S. Müller, R.-J. Zahn, On various kinds of dielectric barrier discharges. *Contr. Plasma Phys.* **36**, 697–709 (1996). <https://doi.org/10.1002/ctpp.2150360606>
6. F. Massines, A. Rabehi, P. Decomps, R.B. Gadri, P. Ségur, C. Mayoux, Experimental and theoretical study of a glow discharge at atmospheric pressure controlled by dielectric barrier. *J. Appl. Phys.* **83**(6), 2950–2957 (1998). <https://doi.org/10.1063/1.367051>
7. F. Massines, P. Ségur, N. Gheradi, C. Khamphan, A. Ricard, Experimental and theoretical study of a glow discharge at atmospheric pressure controlled by dielec-

- tric barrier. *Surf. Coat. Technol.* **174–175**, 8–14 (2003). [https://doi.org/10.1016/S0257-8972\(03\)00540-1](https://doi.org/10.1016/S0257-8972(03)00540-1)
8. E. Aldea, P. Peeters, H. De Vries, M.C.M. Van De Sanden, Atmospheric glow stabilization. Do we need pre-ionization? *Surf. Coat Technol.* **200**(1), 46–50 (2005). <https://doi.org/10.1016/j.surfcoat.2005.01.052>
  9. A. Fridman, A. Chirokov, A. Gutsol, Non-thermal atmospheric pressure discharges. *J. Phys. D: Appl. Phys.* **38**, 1–24 (2005). <https://doi.org/10.1088/0022-3727/38/2/R01>
  10. F. Massines, C. Sarra-Bournet, F. Fanelli, N. Naudé, N. Gherardi, Atmospheric pressure low temperature direct plasma technology: status and challenges for thin film deposition. *Plasma Process. Polym.* **9**, 1041–1073 (2012). <https://doi.org/10.1002/ppap.201200029>
  11. J. Vallade, R. Bazinette, L. Gaudy, F. Massines, Effect of glow DBD modulation on gas and thin film chemical composition: case of Ar/SiH<sub>4</sub>/NH<sub>3</sub> mixture. *J. Phys. D: Appl. Phys.* **47**, 224006 (2014). <https://doi.org/10.1088/0022-3727/47/22/224006>
  12. S. Okazaki, M. Kogoma, M. Uehara, Y. Kimura, Appearance of stable glow discharge in air, argon, oxygen and nitrogen at atmospheric pressure using a 50 Hz source. *J. Phys. D: Appl. Phys.* **26**, 889–892 (1993). <https://doi.org/10.1088/0022-3727/26/5/025>
  13. S.F. Miralá, E. Monette, R. Bartnikas, G. Czere-muszkin, M. Latrèche, M.R. Wertheimer, Electrical and optical diagnostics of dielectric barrier discharges (DBD) in He and N<sub>2</sub> for polymer treatment. *Plasma Polym.* **5**(2), 63–77 (2000). <https://doi.org/10.1023/A:1009531831404>
  14. J.-S. Boisvert, L. Stafford, N. Naudé, J. Margot, F. Massines, Electron density and temperature in an atmospheric-pressure helium diffuse dielectric barrier discharge from kHz to MHz. *Plasma Sources Sci. Technol.* **27**, 035005 (2018). <https://doi.org/10.1088/1361-6595/aab025>
  15. A. Belinger, S. Dap, N. Naudé, Influence of the dielectric thickness on the homogeneity of a diffuse dielectric barrier discharge in air. *J. Phys. D: Appl. Phys.* **55**(46), 465201 (2022). <https://doi.org/10.1088/1361-6463/ac9067>
  16. K.V. Kozlov, R. Brandenburg, H.-E. Wagner, A.M. Morozov, P. Michel, Investigation of the filamentary and diffuse mode of barrier discharges in N<sub>2</sub>/O<sub>2</sub> mixtures at atmospheric pressure by cross-correlation spectroscopy. *J. Phys. D: Appl. Phys.* **38**, 518–529 (2005). <https://doi.org/10.1088/0022-3727/38/4/003>
  17. F. Massines, N. Gherardi, N. Naudé, P. Ségur, Recent advances in the understanding of homogeneous dielectric barrier discharges. *Eur. Phys. J. Appl. Phys.* **47**, 22805 (2009). <https://doi.org/10.1051/epjap/2009064>
  18. R. Tschiersch, M. Bogaczyk, H.-E. Wagner, Systematic investigation of the barrier discharge operation in helium, nitrogen, and mixtures: discharge development, formation and decay of surface charges. *J. Phys. D: Appl. Phys.* **47**, 365204 (2014). <https://doi.org/10.1088/0022-3727/47/36/365204>
  19. R. Brandenburg, Dielectric barrier discharges: progress on plasma sources and on the understanding of regimes and single filaments. *Plasma Sources Sci. Technol.* **26**, 053001 (2017). <https://doi.org/10.1088/1361-6595/aa6426>
  20. S. Nemschokmichal, J. Meichsner, Spatio-temporal characterization of N<sub>2</sub>(A<sup>3</sup>Σ<sub>u</sub><sup>+</sup>) metastables in diffuse nitrogen barrier discharges. *J. Phys. D Appl. Phys.* **48**, 405203 (2015). <https://doi.org/10.1088/0022-3727/48/40/405203>
  21. C. Tyl, X. Lin, M. Bouzidi, S. Dap, H. Caquineau, P. Ségur, N. Gherardi, N. Naudé, Investigation of memory effect in atmospheric pressure dielectric barrier discharge in nitrogen with small oxygen or nitric oxide addition. *J. Phys. D: Appl. Phys.* **51**(35), 354001 (2018). <https://doi.org/10.1088/1361-6463/aad472>
  22. X. Lin, C. Tyl, N. Naudé, N. Gherardi, N.A. Popov, S. Dap, The role of associative ionization reactions in the memory effect of atmospheric pressure townsend discharges in N<sub>2</sub> with a small O<sub>2</sub> addition. *J. Phys. D: Appl. Phys.* **53**(20), 205201 (2020). <https://doi.org/10.1088/1361-6463/ab7518>
  23. P. Bílek, L. Kuthanová, T. Hoder, M. Šimek, Atmospheric pressure townsend discharge in pure nitrogen - a test case for N<sub>2</sub>(A<sup>3</sup>Σ<sub>u</sub><sup>+</sup>, v) kinetics under low E/N conditions. *Plasma Sources Sci. Technol.* (2022). <https://doi.org/10.1088/1361-6595/ac7ad1>
  24. H. Höft, M. Kettlitz, M.M. Becker, R. Brandenburg, Impact of N<sub>2</sub>O admixture on the characteristics of pulsed dielectric barrier discharges in N<sub>2</sub> at atmospheric pressure. *J. Phys. D: Appl. Phys.* **53**, 025203 (2020). <https://doi.org/10.1088/1361-6463/ab4944>
  25. M. Kettlitz, H. Höft, T. Hoder, S. Reuter, K.-D. Weltmann, R. Brandenburg, On the spatio-temporal development of pulsed barrier discharges: influence of duty cycle variation. *J. Phys. D: Appl. Phys.* **45**(24), 245201 (2012). <https://doi.org/10.1088/0022-3727/45/24/245201>
  26. H. Höft, M. Kettlitz, M.M. Becker, T. Hoder, D. Loffhagen, R. Brandenburg, K.-D. Weltmann, Breakdown characteristics in pulsed-driven dielectric barrier discharges: influence of the pre-breakdown phase due to volume memory effects. *J. Phys. D: Appl. Phys.* **47**(46), 465206 (2014). <https://doi.org/10.1088/0022-3727/47/46/465206>
  27. M.M. Becker, T. Hoder, R. Brandenburg, D. Loffhagen, Analysis of microdischarges in asymmetric dielectric barrier discharges in argon. *J. Phys. D: Appl. Phys.* **46**, 355203 (2013). <https://doi.org/10.1088/0022-3727/46/35/355203>
  28. M.M. Becker, D. Loffhagen, Enhanced reliability of drift-diffusion approximation for electrons in fluid models for nonthermal plasmas. *AIP Advances* **3**, 012108 (2013). <https://doi.org/10.1063/1.4775771>
  29. A. Kossyi, A.Y. Kostinsky, A.A. Matveyev, V.P. Silakov, Kinetic scheme of the nonequilibrium discharge in nitrogen-oxygen mixtures. *Plasma Sources Sci. Technol.* **1**, 207–220 (1992). <https://doi.org/10.1088/0963-0252/1/3/011>
  30. J. Marbach, F.X. Bronold, H. Fehske, Resonant charge transfer at dielectric surfaces electron capture and release due to impacting metastable nitrogen molecules. *Eur. Phys. J. D* **66**, 106 (2012). <https://doi.org/10.1140/epjd/e2012-30014-8>
  31. G.J.M. Hagelaar, F.J. de Hoog, G.M.W. Kroesen, Boundary conditions in fluid models of gas discharges. *Phys. Rev. E* **62**, 1452–1454 (2000). <https://doi.org/10.1103/PhysRevE.62.1452>

32. Y.P. Raizer, *Gas Discharge Physics* (Springer, Berlin, Heidelberg, 1991)
33. F. Massines, N. Gherardi, N. Naudé, P. Ségur, Glow and Townsend dielectric barrier discharge in various atmosphere. *Plasma Phys. Control. Fusion* **47**(12B), 577 (2005). <https://doi.org/10.1088/0741-3335/47/12B/S42>
34. J.R. Wubs, H. Höft, M. Kettlitz, M.M. Becker, K.-D. Weltmann, Impact of the electrode proximity on the streamer breakdown and development of pulsed dielectric barrier discharges. *Plasma Sources Sci. Technol.* **31**(3), 035006 (2022). <https://doi.org/10.1088/1361-6595/ac511f>
35. N. Naudé, J.-P. Cambronne, N. Gherardi, F. Massines, Electrical model and analysis of the transition from an atmospheric pressure townsend discharge to a filamentary discharge. *J. Phys. D: Appl. Phys.* **38**, 530–538 (2005). <https://doi.org/10.1088/0022-3727/38/4/004>
36. R. Brandenburg, V.A. Maiorov, Y.B. Golubovskii, H.-E. Wagner, J. Behnke, J.F. Behnke, Diffuse barrier discharges in nitrogen with small admixtures of oxygen: discharge mechanism and transition to the filamentary regime. *J. Phys. D: Appl. Phys.* **38**, 2187–2197 (2005). <https://doi.org/10.1088/0022-3727/38/13/017>
37. R. Brandenburg, M. Bogaczyk, H. Höft, S. Nemschokmichal, R. Tschiersch, M. Kettlitz, L. Stollenwerk, T. Hoder, R. Wild, K.-D. Weltmann, J. Meichsner, H.-E. Wagner, Novel insights into the development of barrier discharges by advanced volume and surface diagnostics. *J. Phys. D: Appl. Phys.* **46**, 464015 (2013). <https://doi.org/10.1088/0022-3727/46/46/464015>
38. U. Kogelschatz, Dielectric-barrier discharges: their history, discharge physics, and industrial applications. *Plasma Sources Sci. Technol.* **23**, 1–46 (2003). <https://doi.org/10.1023/a:1022470901385>
39. M. Kettlitz, H. Höft, T. Hoder, K.-D. Weltmann, R. Brandenburg, Comparison of sinusoidal and pulsed-operated dielectric barrier discharges in an O<sub>2</sub>/N<sub>2</sub> mixture at atmospheric pressure. *Plasma Sources Sci. Technol.* **22**(2), 025003 (2013). <https://doi.org/10.1088/0963-0252/22/2/025003>
40. G. Steinle, D. Neundorf, W. Hiller, M. Pietralla, Two-dimensional simulation of filaments in barrier discharges. *J. Phys. D: Appl. Phys.* **32**, 1350 (1999). <https://doi.org/10.1088/0022-3727/32/12/311>
41. S. Nemschokmichal, R. Tschiersch, H. Höft, R. Wild, M. Bogaczyk, M.M. Becker, D. Loffhagen, L. Stollenwerk, M. Kettlitz, R. Brandenburg, J. Meichsner, Impact of volume and surface processes on the pre-ionization of dielectric barrier discharges: advanced diagnostics and fluid modeling. *Eur. Phys. J. D* **72**, 89 (2018). <https://doi.org/10.1140/epjd/e2017-80369-1>
42. H. Höft, M. Kettlitz, K.-D. Weltmann, R. Brandenburg, The bidirectional character of O<sub>2</sub> concentration in pulsed dielectric barrier discharges in O<sub>2</sub>/N<sub>2</sub> gas mixtures. *J. Phys. D: Appl. Phys.* **47**(45), 455202 (2014). <https://doi.org/10.1088/0022-3727/47/45/455202>
43. T. Hoder, H. Höft, M. Kettlitz, K.-D. Weltmann, R. Brandenburg, Barrier discharges driven by sub-microsecond pulses at atmospheric pressure: breakdown manipulation by pulse width. *Phys. Plasmas* **19**, 070701 (2012). <https://doi.org/10.1063/1.4736716>
44. E.L. Chaney, L.G. Christophorou, Electron attachment to N<sub>2</sub>O. *J. Chem. Phys.* **51**, 883–892 (1969). <https://doi.org/10.1063/1.1672152>